Imaging Spatial Correlations of Rydberg Excitations in Cold Atom Clouds

A. Schwarzkopf, R. E. Sapiro, and G. Raithel

Phys. Rev. Lett. **107**, 103001 — Published 31 August 2011

DOI: 10.1103/PhysRevLett.107.103001

Imaging spatial correlations of Rydberg excitations in cold atom clouds

A. Schwarzkopf, R. E. Sapiro, and G. Raithel
FOCUS Center, Department of Physics, University of Michigan, Ann Arbor, MI 48109

We use direct spatial imaging of cold ^{85}Rb Rydberg atom clouds to measure the Rydberg-Rydberg correlation function. The results are in qualitative agreement with theoretical predictions [F. Robicheaux and J. V. Hernández, Phys. Rev. A **72**, 063403 (2005)]. We determine the blockade radius for states $44D_{5/2}$, $60D_{5/2}$, and $70D_{5/2}$, and investigate the dependence of the correlation behavior on excitation conditions and detection delay. Experimental data hint at the existence of long range order.

PACS numbers: 32.80.Ee,32.80.Rm,34.20.Cf

When cold atoms are laser-excited to Rydberg states, the strong interactions between Rydberg excitations can lead to complex many-body entanglement in the system. The excitation process results in spatial correlations between excitations in the system. In most cases, Rydberg excitation positions are anticorrelated such that no two excitations are within a "blockade radius" $r_{\rm b}$ of each other. Such systems are well-suited for studying basic many-body physics [1–3], as well as for future technological applications such as quantum computation [4, 5]. Theory for the laser excitation process that leads to the Rydberg blockade is considered in Refs. [6, 7]. Previous experiments have shown the blockade effect to cause a suppression of excitation in an atom sample [8] and sub-Poissonian excitation-number statistics [9]. The underlying energy level shifts were measured spectroscopically [10].

We are presently interested in the spatial aspect of the blockade. In spatially-resolved studies the distance-[11] and angle-dependence [12] of Rydberg-Rydberg interactions were examined. The blockade effect was shown to be effective between spatially separated atom pairs in adjacent dipole traps [13, 14]. In this paper we directly image a system containing multiple Rydberg excitations to obtain the Rydberg-Rydberg correlation function. We find evidence of the Rydberg excitation blockade and measure the blockade radius for several principal quantum numbers n.

The experimental setup is sketched in Fig. 1. The key feature enabling spatial resolution of the Rydberg sample is the ionization electrode: a beryllium-copper needle with a rounded tip of diameter 125 μm. This tip imaging probe (TIP) is surrounded by a closed cage of electrodes whose voltages can be controlled to a precision of several millivolts. These electrodes allow independent control of the electric field in three orthogonal directions. To provide temporal and spatial electric-field stability, the apertures in the electrodes are covered with wire mesh which has 0.51 mm grid spacing and 88% transparency.

The experiment runs at a repetition rate of 30 Hz. We collect ^{85}Rb atoms for about 30 ms in a MOT located ∼500 μm above the TIP. After turning off the MOT light, we optically pump the ground state atoms into the $5S_{1/2}|F=3, m_{\rm F}=3\rangle$ state, with the quantization axis along the beam direction. We then excite

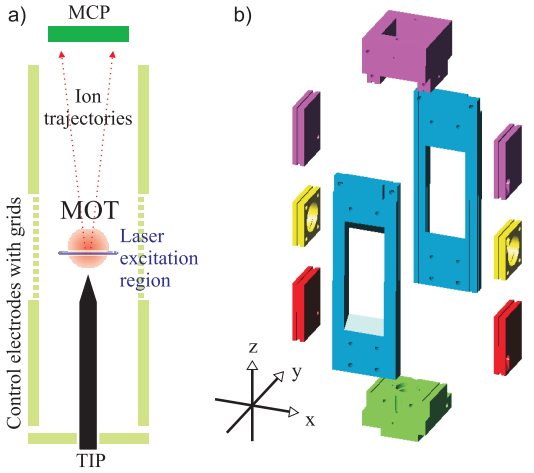

FIG. 1. (color online) (a) Overview of excitation region and ion detection. (b) Exploded view of electrodes that surround the excitation region, used for electric field control. The purple, blue, and yellow electrodes allow electric-field control in the z, y, and x directions, respectively. Green and red electrodes are grounded.

Rydberg atoms in a two-step process, using counter-propagating 480 nm and 780 nm beams. The excitation region is ∼360 μm above the TIP. The beams are σ^+ polarized and resonantly drive the transitions $5S_{1/2}|F=3, m_{\rm F}=3\rangle \rightarrow 5P_{3/2}|F'=4, m'_{\rm F}=4\rangle \rightarrow nD_{5/2}|F''=5, m''_{\rm F}=5\rangle$. The red beam has a Gaussian beam parameter of $w=0.75$ mm, while the blue beam is focused to $w_0 \lesssim 8$ μm with a theoretical confocal parameter of 0.3 mm. Because of the much larger size of the red beam, the intermediate-state population is uniform across the width of the excitation region. We establish with CCD imaging that the intensity distribution of the blue focus is only weakly altered by diffraction from the mesh. Laser linewidths are of order 1 MHz. Typical Rydberg atom densities are $\sim 10^9$ cm^{-3}, dependent on atomic state and laser power.

After excitation, the TIP is switched to high voltage to produce a strong, radially divergent electric field. This field ionizes the Rydberg atoms, and the ions are extracted along the divergent field lines. The ions are detected approximately 15 cm away by a microchannel

plate detector (MCP) which has a spatial resolution of $\gtrsim$ 10 lines/mm. The method resembles field ion microscopy, and leads to magnified ion images of the initial Rydberg atom locations. This image is captured by a CCD video camera, synchronized with the experiment.

In most cases we use 100 ns excitation pulses with a subsequent negligible delay before the field ionization pulse. Under these conditions the atoms can be considered "frozen" in space during the experiment. These parameters are later varied to study their effect on the Rydberg-Rydberg correlation function.

To observe an excitation blockade, it is essential to avoid electric fields during the excitation pulse. Electric fields would cause undesired modifications of the Rydberg-Rydberg interaction potentials. Furthermore, electric field inhomogeneity would induce inhomogeneous line broadening and alter the many-body energy level spectrum, potentially breaking the excitation blockade. By measuring the Stark spectra of nD-manifolds as a function of the potentials on the TIP and the electrodes shown in Fig 1, we zero the electric field to below $\sim$100 mV/cm. This is low enough to avoid the aforementioned problems [15].

The system's magnification factor is determined by the combined ion-lensing effects of the TIP, pulsed to about 400 V, and the MCP front plate, held at -800 V. To calibrate the magnification we scan the focused 480nm beam laterally across the MCP field of view by using a mirror with a piezo actuator on the horizontal axis. Using the known physical displacement of the beam, we determine the scale in the MCP picture. We find a linear magnification factor of 45x between the excitation region and the MCP front surface. 1 μm in the excitation region corresponds to 2.2 pixels in the digital CCD images, with an uncertainty of 10%.

The procedure of data acquisition and processing begins with taking 10000 CCD images of the MCP phosphor screen, each image showing the ion impact positions for a single experimental cycle (as in Fig. 2(a)). A CCD image consists of these blips plus background noise from the camera. To eliminate the background, we determine the maximum background level and subtract it from the image, setting all negatives to zero. This procedure yields filtered images, denoted by X (Fig. 2(b)). The autocorrelation of each filtered image is calculated, and is denoted A. The individual autocorrelations A are then added to construct $\bar{A}$ (Fig. 2(d)). We can write this as follows, using subscripts for the pixel coordinates and superscript α to enumerate the images:

$$A^{\alpha}_{\mathrm{i,j}} = f(\mathrm{i,j},N,M)\sum_{\mathrm{n,m}} X^{\alpha}_{\mathrm{n,m}} X^{\alpha}_{\mathrm{n-i,m-j}} \qquad (1)$$

$$\bar{A}_{\mathrm{i,j}} = \sum_{\alpha} A^{\alpha}_{\mathrm{i,j}} \quad , \qquad (2)$$

where

$$f(\mathrm{i,j},N,M) = \frac{NM}{(N-|i|)(M-|j|)} \quad , \qquad (3)$$

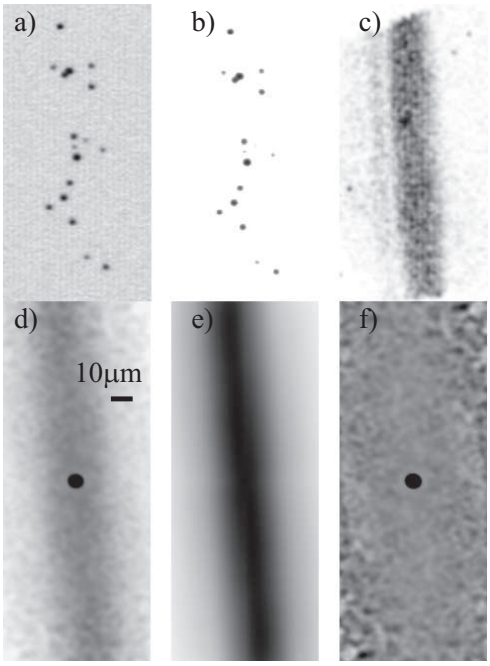

FIG. 2. Stages in the image analysis process, using state $44D_{5/2}$. All have same scale. (a) Raw image (cropped), (b) filtered image, X, (c) sum of filtered images, (d) sum of autocorrelations, $\bar{A}$, (e) autocorrelation of sum of images, B, (f) normalized autocorrelation, $\bar{A}^1$.

$N \times M$ is the image size, and (i,j) is the displacement. The normalization factor f eliminates finite-array effects in Eqs. 2 and 4, as it causes flat images to have flat autocorrelation functions rather than pyramidal ones.

The signal $\bar{A}$ has three main structures: a central peak due to the correlation of a blip with itself, an overall cigar shape due to the geometry of the excitation region, and structure due to correlations between ion positions. It is this third structure that we wish to isolate in our analysis. The raw autocorrelation $\bar{A}$ is useful for qualitative analysis, as it is the easiest to interpret by eye. However, for quantitative analysis we must eliminate the shape of the beam. To do so we first sum the images (Fig. 2(c)) and take the autocorrelation (Fig. 2(e)):

$$B_{\mathrm{i,j}} = f(\mathrm{i,j},N,M)\sum_{\mathrm{n,m}} \left(\sum_{\alpha} X^{\alpha}_{\mathrm{n,m}}\right)\left(\sum_{\beta} X^{\beta}_{\mathrm{n-i,m-j}}\right). \qquad (4)$$

The autocorrelation B does not contain any information about Rydberg-Rydberg correlations, but still shows the overall shape of the excitation region. This allows us to divide out the beam shape by defining a normalized $\bar{A}^1$,

$$\bar{A}^1_{\mathrm{i,j}} = \bar{A}_{\mathrm{i,j}}/N_{\mathrm{p}}B_{\mathrm{i,j}} \quad , \qquad (5)$$

where N_{p} is the number of pictures in the dataset. The normalization of $\bar{A}^1$ is such that a value > 1 (< 1) should indicate a correlation (anticorrelation) of ion positions.

We take data at several combinations of red and blue laser powers. For the intensity of the lower transition

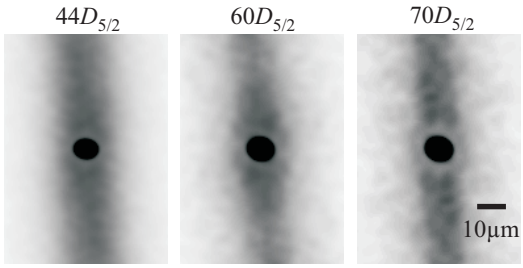

FIG. 3. Autocorrelations $\bar{A}$ for $44D_{5/2}$, $60D_{5/2}$, and $70D_{5/2}$. In the datasets shown we use a laser intensity of 3.4 $I_{\rm sat}$ for the lower transition, and the lowest intensity setting (nearest the saturation knee) for the upper transition.

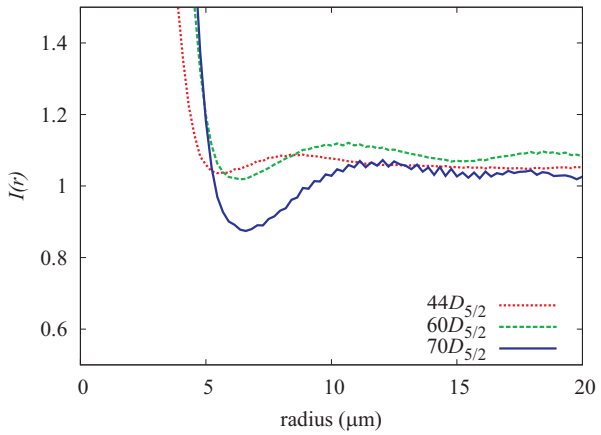

FIG. 4. (color online) Angular average of $\bar{A}^1$, $I(r)$, for $44D_{5/2}$, $60D_{5/2}$, and $70D_{5/2}$. Curves correspond to images in Fig. 3.

beam we use intensities of 1.7 $I_{\rm sat}$ and 3.4 $I_{\rm sat}$, where the saturation intensity $I_{\rm sat} = 1.6$ mW/cm^2. For each of these intensities we measure the atom number as a function of the intensity of the upper transition beam and observe saturation behavior as in Ref. [8]. To acquire images for the autocorrelation analysis described above, we select several intensities of the upper transition beam around and beyond the knee of the measured saturation curves. We find that the autocorrelations nearest the knee tend to show the clearest correlation-induced structures.

Figure 3 shows $\bar{A}$ measured for states $44D_{5/2}$, $60D_{5/2}$, and $70D_{5/2}$. For all three states, we observe a ring-shaped dip around the central self-correlation peak in the autocorrelation. Such dips are present in most of our data, with the degree of visibility depending on excitation parameters. The absence of dips in some data indicates that they are not artifacts of the imaging or image processing. We find that laser frequency fluctuations can make the dips change in depth and diameter. Furthermore, laser power affects the results, as described below.

To quantitatively compare the autocorrelations $\bar{A}^1$ of different states, in Fig. 4 we plot $I(r)$, defined as the angular average of $\bar{A}^1$. $I(r)$ is analogous to the radial autocorrelation function calculated in Ref. [6]. The self-term fills the region $r < 5$ μm. We do not remove the self term due to the risk of producing a false blockade signal. Between 5 and 10 μm, each curve has a dip indicating an anticorrelation in Rydberg atom positions, as was qualitatively observed in Fig. 3. The minima of $I(r)$ do not approach zero in part because we are projecting a 3-dimensional sample onto the detector plane, which reduces the visibility for even a perfect blockade.

Figure 4 shows that the blockade radius increases with principal quantum number n. However, there is no obvious choice for a method to measure a blockade radius from each curve, as the curve's shape is determined by both the blockade-induced dip and the self-term.

To determine a good measure for the blockade radius, we simulate the excitation/blockade process for our geometry and z-projection conditions, using a stochastic, non-quantum model. We find that the inflection point after the minimum of each $I(r)$ curve is close to the input hard-sphere blockade radius. We thus use this inflection point as our measure of the blockade radius. We note that in the simulations the self-term diminishes the dip depth and can shift the dip position. If the input blockade radius is close to the self-term width, the radius indicated by the inflection point is 1–2 μm higher than the blockade radius. When the blockade radius is much larger than the self-term width, the inflection point method underestimates the input blockade radius by $\lesssim$1 μm.

For the states $44D_{5/2}$, $60D_{5/2}$, and $70D_{5/2}$ we measured the radii on nine, six, and nine curves. One additional curve was discarded for $70D_{5/2}$; although its dip minimum was consistent with other data, the position of its inflection point was unclear. Five additional curves for $44D_{5/2}$ were thrown out because there was no dip, as discussed below. The measured blockade radii are shown in Fig. 5. The error bars indicate the 10% uncertainty from the magnification calibration; this systematic uncertainty dominates the uncertainty due to measurement statistics by a factor of at least two.

In Fig. 5 we compare the measurements to predictions based on an excitation bandwidth $\delta\nu_{\rm L}$ ranging from 5 to 12 MHz and interaction strengths as determined from Ref. [15]. The blockade radius for the van der Waals interaction has been calculated to be

$$r_{\rm b} \approx \left[\frac{\Delta\tilde{W}^{(2)}(n^*)^{11}}{h(\delta\nu_{\rm L})}\right]^{1/6}, \qquad (6)$$

where $n^* = n - \delta_l$ is the effective principal quantum number, δ_l is the quantum defect, and $\Delta\tilde{W}^{(2)}$ is a scaled, second-order, state-dependent van der Waals coefficient defined in Ref [15]. $\Delta\tilde{W}^{(2)}$ is scaled such that it would be independent of n^* in the absence of resonant level shifts. The assumed value for $\delta\nu_{\rm L}$ has little effect due to the sixth-root dependence.

Figure 5 shows that the measured blockade radii are within a factor of two of the predictions. Further, the amount by which the blockade radius increases between

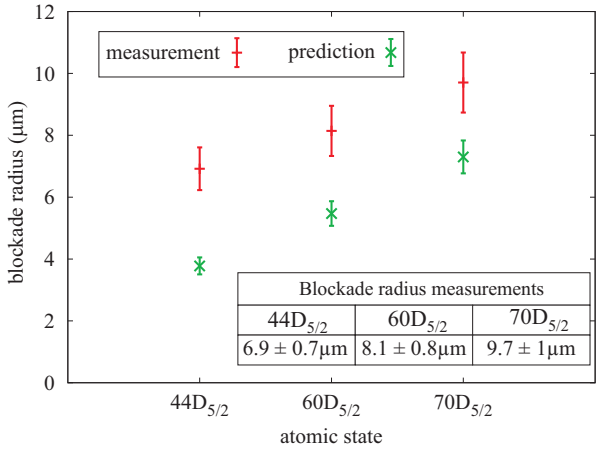

FIG. 5. (color online) Comparison of blockade radius measurements (+) with predictions (×) based on Ref. [15].

the probed n levels is as expected. The measured blockade radii exceed the calculated radii by 2–3 μm. The difference may be because Eq. 6 models the interaction between two atoms and excludes many-body effects [3]. Ates *et al.* have previously seen evidence that theory based on pair-wise interactions underestimates the blockade radius [7].

To test if atomic motion or the degree of excitation saturation modifies the observed correlation behavior, we vary laser powers, excitation pulse duration, and field extraction delays. In general, increasing the laser power, or the excitation duration at constant power, diminishes the dip depth (defined as the curve asymptote minus the dip minimum). For instance, increasing the excitation duration for state $70D_{5/2}$ from 100 ns to 400 ns causes the dip depth to decrease from 0.24 to 0.04. This behavior could be caused by an increased z-depth of the saturated part of the excitation region. In our simulations the degree to which the dip depth is diminished depends on the assumed beam focus quality. Adding wings to a Gaussian focus, as suggested by Fig. 2(c), yields better qualitative agreement with our data.

Laser power has a greater effect for the case of excitation to $44D_{5/2}$ than for the other states: in five $I(r)$ curves the dip disappeared entirely. We expect this is partly due to saturating the atomic transition for $44D_{5/2}$ more strongly than for $60D_{5/2}$ or $70D_{5/2}$. It is also possible that, of the three states we studied, $44D_{5/2}$ is the most susceptible to laser parameters due to having the shallowest dip, closest to the radius of the self-term. Another possibility is that the blockade efficiency is diminished due to the proximity of the Förster resonance, as suggested by Refs. [3, 16].

By varying the delay between excitation and field ionization we test the longevity of the correlations. They are remarkably long-lived. The dip depth decreases by about half over 10 μs, despite possible atomic motion and ionization during this time [17, 18]. This result awaits a future theoretical explanation.

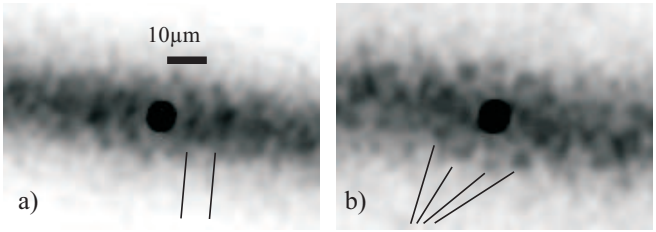

FIG. 6. Some autocorrelations ($\bar{A}$) showing possible long-range and angular structure for state $44D_{5/2}$.

Some of our data, using linear laser polarization and a few MHz of detuning, show additional structures. The autocorrelation in Fig. 6(a) exhibits multiple rings, indicating long-range Rydberg-Rydberg correlations. The autocorrelation in Fig. 6(b) hints at multiple maxima in a ring about the center, indicating possible angular dependence of the Rydberg-Rydberg correlation function. There have been predictions of crystal-like structure in Rydberg systems [19], but the detailed excitation conditions are important in generating these structures. At present we are working to improve our experimental control in order to systematically study these effects.

In summary, we have obtained spatially-resolved images of blockaded Rydberg atom samples and evaluated the Rydberg-Rydberg correlation function. Having observed a blockade, we measured the blockade radius for several quantum states. We have also tested the dependence of the blockade on parameters such as laser power, excitation duration, and detection delay. Future work could include investigation of longer range correlation structures, extending beyond one blockade radius, as in Fig. 6. One could further attempt to excite a Rydberg crystal as proposed in Ref. [19].

We acknowledge the help of Dr. Brenton Knuffman in the design phase of the experiment. This work was supported by the NSF (PHY-0855871), AFOSR (FA9550-10-1-0453), and FOCUS (PHY-0114336).

[1] I. Mourachko *et al.*, Phys. Rev. Lett. **80**, 253 (1998).
[2] P. J. Tanner *et al.*, Phys. Rev. Lett. **100**, 043002 (2008).
[3] K. C. Younge *et al.*, Phys. Rev. A **79**, 043420 (2009).
[4] M. D. Lukin *et al.*, Phys. Rev. Lett. **87**, 037901 (2001).
[5] D. Jaksch *et al.*, Phys. Rev. Lett. **85**, 2208 (2000).
[6] F. Robicheaux and J. V. Hernández, Phys. Rev. A **72**, 063403 (2005).
[7] C. Ates *et al.*, Phys. Rev. A **76**, 013413 (2007).
[8] D. Tong *et al.*, Phys. Rev. Lett. **93**, 063001 (2004).
[9] A. Reinhard, K. C. Younge, and G. Raithel, Phys. Rev.

A **78**, 060702 (2008).
[10] A. Reinhard *et al.*, Phys. Rev. Lett. **100**, 233201 (2008).
[11] C. S. E. van Ditzhuijzen *et al.*, Phys. Rev. Lett. **100**, 243201 (2008).
[12] T. J. Carroll *et al.*, Phys. Rev. Lett. **93**, 153001 (2004).
[13] A. Gaetan *et al.*, Nat Phys **5**, 115 (2009).
[14] E. Urban *et al.*, Nat Phys **5**, 110 (2009).
[15] A. Reinhard *et al.*, Phys. Rev. A **75**, 032712 (2007).
[16] T. G. Walker and M. Saffman, J. Phys. B **38**, S309 (2005).
[17] T. Amthor *et al.*, Phys. Rev. Lett. **98**, 023004 (2007).
[18] F. Robicheaux, J. Phys. B **38**, S333 (2005).
[19] T. Pohl, E. Demler, and M. D. Lukin, Phys. Rev. Lett. **104**, 043002 (2010).